Beyond the Rabi model: Light interactions with polar atomic systems in a cavity

Giovanni Scala,[1,2,3] Karolina Słowik,[4,*] Paolo Facchi,[1,2] Saverio Pascazio,[1,2] and Francesco V. Pepe[1,2]

[1]*Dipartimento Interateneo di Fisica, Università degli Studi di Bari, I-70126 Bari, Italy*

[2]*INFN, Sezione di Bari, I-70125 Bari, Italy*

[3]*International Centre for Theory of Quantum Technologies (ICTQT), University of Gdansk, Wita Stwosza 63, 80-308 Gdańsk, Poland*

[4]*Institute of Physics, Faculty of Physics, Astronomy and Informatics, Nicolaus Copernicus University in Toruń, Grudziadzka 5/7, 87-100 Torun, Poland*

(Received 23 March 2021; revised 25 May 2021; accepted 9 July 2021; published 27 July 2021)

The Rabi Hamiltonian, describing the interaction between a two-level atomic system and a single-cavity mode of the electromagnetic field, is one of the fundamental models in quantum optics. The model becomes exactly solvable by considering an atom without permanent dipole moments, whose excitation energy is quasiresonant with the cavity photon energy, and by neglecting the nonresonant (counter-rotating) terms. In this case, after including the decay of either the atom or the cavity mode to a continuum, one can derive the well-known phenomenology of quasiresonant transitions, including the fluorescence triplets. In this work we consider the most general Rabi model, incorporating the effects of permanent atomic electric dipole moments. Based on a perturbative analysis, we compare the intensities of emission lines induced by rotating terms, counter-rotating terms, and parity-symmetry-breaking terms in order to identify the parameter regimes in which these different contributions play a significant role. The analysis reveals that the emission strength related to the existence of permanent dipoles may surpass the one due to the counter-rotating interaction terms but is usually much weaker than the emission due to the main, resonant coupling. This ratio can be modified in systems with a reduced dimensionality or by engineering the energy spectral density of the continuum.

DOI: 10.1103/PhysRevA.104.013722

I. INTRODUCTION

The Rabi model is a fundamental tool in quantum optics. It describes the coupling of a two-level system and a bosonic field mode [1], extending beyond the simpler Jaynes-Cummings interaction, in which the creation of a photon is always accompanied by annihilation of the atomic excitation and vice versa [2]. The Rabi model additionally accounts for the less intuitive processes of pairwise creation or annihilation of excitations in the atomic and photonic subsystems. The probability of these processes grows with the light-matter coupling constant and becomes significant in the so-called ultrastrong coupling regime in which the coupling constant becomes comparable to the energy of the system [3]. Numerous experimental realizations include superconducting systems [4,5], quantum wells [6,7], photonic waveguide arrays [8], molecular ensembles [9], cold atoms [10], etc. In all these systems the extension beyond the Jaynes-Cummings interaction may lead to considerably different physics: in particular, to a ground state with a nonvanishing number of excitations, squeezing dynamic, and a significant modification of the spectra [1,11,12]. Different approaches to solve the Rabi model and its extensions are based on exploiting discrete symmetries [11], Bogoliubov operators [12], polaron transformation [13,14], the generalized rotating-wave approximation [15], and perturbative approach [16,17].

The Rabi model describes light-matter interaction, where the electromagnetic field induces transitions between the eigenstates of a two-level atomic system. A particular mechanism is related to a coupling of the electromagnetic radiation with a transition dipole moment element induced between a pair of atomic eigenstates. However, simple two-level systems may display versatile physical features, beyond the traditional Rabi model: a particular example is a coupling scenario where the electromagnetic field introduces energy shifts of the eigenstates rather than transitions between them [18,19]. A simple realization exploits atomic systems with permanent dipole moments, such as polar molecules or asymmetric quantum dots. Due to the interplay of permanent and induced electric dipole moments, polar systems are a playground where a richer physics of light-matter interactions can be realized: polar quantum systems have been proposed for THz radiation sources [18] based on quantum dots [20] or molecular ensembles [21]. They can be exploited for squeezed light generation [22,23], and they support light-matter entanglement [24] and nonlinear optical absorption [19]. Recently, the impact of spatial asymmetry of a quantum system on its spontaneous emission properties has been investigated [25].

The aforementioned works are among the plethora of possibilities provided by asymmetric quantum systems that simultaneously support light-matter interactions through three types of terms. These include the Jaynes-Cummings terms and the counter-rotating terms, both involving transition dipole moments of the atomic system. The third type of terms involves permanent dipoles, i.e., nonvanishing expectation values of the dipole moment operator in the atomic

*karolina@fizyka.umk.pl

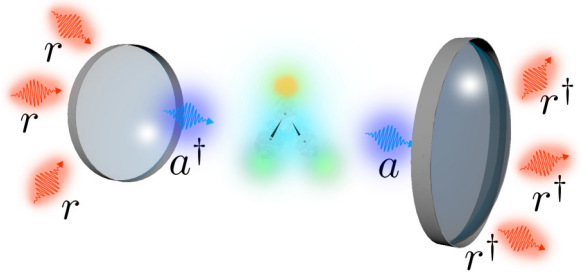

FIG. 1. Sketch of the system under study: a two-level polar atomic system in a lossy cavity represented by two semitransparent mirrors. The nonuniform charge distribution is shown as blurred clouds: two green clouds at the bottom of the molecule for a higher concentration of positive charges and in the orange cloud at the top for the negative charges. The annihilation and creation operators of the electromagnetic modes are denoted as a, $a^\dagger$ for the cavity (represented as blue wave packets inside the cavity) and r, $r^\dagger$ for the reservoir (red wave packets outside).

eigenstates. For the numerous applications listed above it is essential to identify conditions in terms of experimentally tunable model parameters where different contributions significantly influence the system's optical response. This work aims to study the relative impact of these three contributions and demonstrate with simple examples the possibility of performing density-of-states engineering. Our analysis follows the methodology introduced in Ref. [17] but extends it to include all three interaction mechanisms.

The paper is organized as follows: A two-level atomic system without inversion symmetry, coupled to a single-mode electromagnetic field, is introduced in Sec. II. Next, we apply a perturbative framework to find a ladder of eigenstates and the corresponding energies in Sec. III. Transitions between these eigenstates upon coupling with an external lossy cavity are described in Sec. IV, which ends the analytical part. Numerical examples of systems with low-to-moderate light-matter coupling strengths are given in Sec. V. In Appendix A we discuss the validity of the perturbative approach, while details of calculations of the spectral distribution of emitted photons are given in Appendix B.

II. HAMILTONIAN OF THE SYSTEM

Let us consider a two-level system with ground and excited state respectively denoted as $|g\rangle$, $|e\rangle$, separated by the excitation energy $\hbar\omega_a$. The system, pictorially represented in Fig. 1, is described by the set of Pauli operators

$$\sigma_- = |g\rangle\langle e|, \quad \sigma_+ = |e\rangle\langle g|, \tag{1}$$

$$\sigma_z = |e\rangle\langle e| - |g\rangle\langle g|. \tag{2}$$

This system interacts with a single electromagnetic cavity mode, represented by the field operators a and $a^\dagger$, satisfying the canonical commutation algebra

$$[a, a^\dagger] = 1, \quad [a, a] = [a^\dagger, a^\dagger] = 0. \tag{3}$$

The Hamiltonian H of the coupled system can be divided into two parts,

$$H = H_{\rm JC} + V, \tag{4}$$

with the first term

$$H_{\rm JC} = \hbar\omega_c a^\dagger a + \frac{\hbar\omega_a}{2}\sigma_z + \hbar g_R(\sigma_+ a + a^\dagger\sigma_-), \tag{5}$$

known as the Jaynes-Cummings (JC) Hamiltonian [2], that describes quasiresonant transitions between the atomic excitations and photons. Here, g_R is the coupling strength of the resonant JC term. The results in the following analysis are independent of the coupling mechanism and the specific expressions of the coupling constants in terms of microscopic parameters. In the case of an atom coupled to one mode of a three-dimensional (3D) rectangular cavity, the coupling constant reads $g_R = -\boldsymbol{d}_{\rm eg}\cdot\boldsymbol{\epsilon}\sqrt{\hbar\omega_c/2\epsilon_0\mathcal{V}}$, where $\boldsymbol{d}_{\rm eg} = \langle e|\boldsymbol{d}|g\rangle$ represents the off-diagonal matrix element of the electric dipole operator $\boldsymbol{d}$ of the atom, $\boldsymbol{\epsilon}$ is the polarization vector of the cavity mode, ϵ_0 the vacuum electric permittivity, and $\mathcal{V}$ the cavity volume.

The "perturbation" term V in Eq. (4) accounts for all the terms that are not represented in the exactly solvable Jaynes-Cummings Hamiltonian, namely, the counter-rotating (CR) transitions between atom and cavity excitations and the terms proportional to the diagonal matrix elements of the atomic dipole moment:

$$V = H_{\rm CR} + H_{\rm AS}, \tag{6}$$

$$H_{\rm CR} = \hbar g_R(\sigma_+ a^\dagger + \sigma_- a), \tag{7}$$

$$H_{\rm AS} = \hbar[g_S(\sigma_z + \mathbf{1}) + g'_S(\sigma_z - \mathbf{1})](a + a^\dagger), \tag{8}$$

with

$$g_S = -\boldsymbol{d}_{\rm ee}\cdot\boldsymbol{\epsilon}\sqrt{\hbar\omega_c/8\epsilon_0\mathcal{V}}, \tag{9}$$

$$g'_S = -\boldsymbol{d}_{\rm gg}\cdot\boldsymbol{\epsilon}\sqrt{\hbar\omega_c/8\epsilon_0\mathcal{V}}, \tag{10}$$

proportional to the expectation values of the atomic dipole moment on the excited and ground state, respectively. In this article, we focus specifically on the case $g'_S = 0$.

Note that the expectation value of a dipole moment operator described only by off-diagonal elements $\boldsymbol{d}_{\rm eg}|e\rangle\langle g| + \boldsymbol{d}^*_{\rm eg}|g\rangle\langle e|$ may be nonzero only in the presence of transitions between the eigenstates that may be induced with the external electric field; therefore, these elements correspond to induced transition dipoles. On the other hand, the diagonal element describes the permanent dipole moment of the excited state. Notably, permanent dipole moments are sustained by polar systems, i.e., systems without inversion symmetry [18]. For this reason, we will refer to the last Hamiltonian term as the "asymmetry term" or "diagonal term" and mark it with the AS subscript. Finally, note that while the Hamiltonian $H_{\rm JC}$ preserves the number of excitations, $H_{\rm AS}$ ($H_{\rm CR}$) describes a modification of this number by 1 (respectively 2).

III. PRELIMINARIES: PERTURBATIONS OF THE JAYNES-CUMMINGS HAMILTONIAN

In the following analysis we will treat V as a perturbation with respect to the Hamiltonian $H_{\rm JC}$. The results generalize and encompass those derived in Refs. [16,17] for more specific Hamiltonians. The eigenvalues of $H_{\rm JC}$ correspond to the

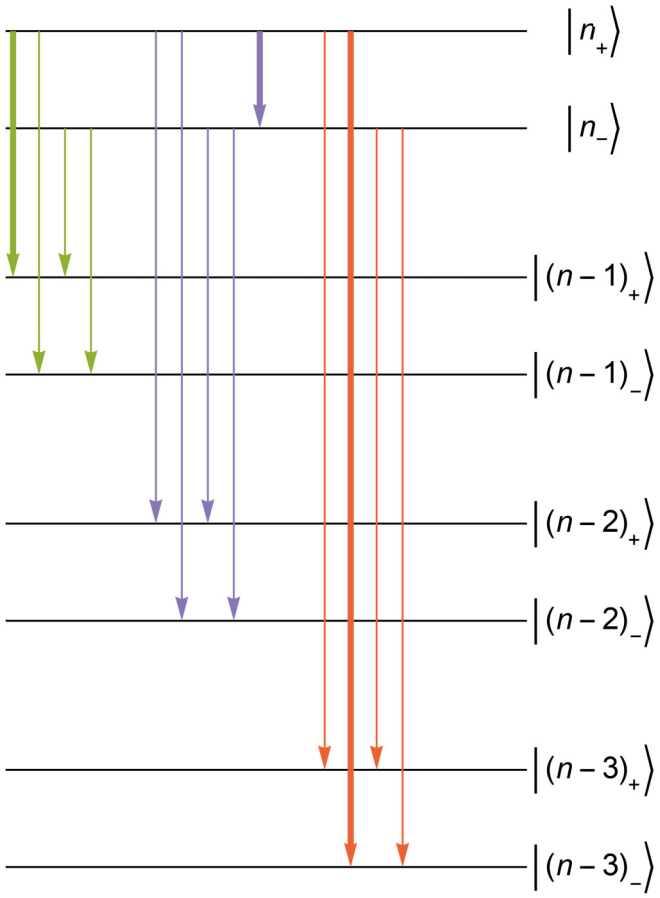

FIG. 2. From left to right, the first set of transitions (green) involves four decay channels from the $\mathcal{E}(n)$ to the $\mathcal{E}(n-1)$ manifold and is allowed by $H_{\rm JC}$, as expressed in Eq. (29). The next set of five new transition lines (violet) towards $n' = n$ and $n' = n-2$ originate at $H_{\rm AS}$. Transitions due to the counter-rotating Hamiltonian $H_{\rm CR}$ (red) connect manifold $\mathcal{E}(n)$ to $\mathcal{E}(n-3)$. The three thicker lines are studied in more detail in Fig. 5.

0th-order perturbation term

$$E_n^{s(0)} = \hbar\omega_c\left(n-\frac{1}{2}\right) + s\hbar\sqrt{\frac{(\omega_c-\omega_a)^2}{4} + ng_R^2} \tag{11}$$

for $n = 0, 1, \ldots$ and $s = \pm 1$, and the eigenstates are

$$\left|n_s^{(0)}\right\rangle = A_n^s|g;n\rangle + B_n^s|e,n-1\rangle, \tag{12}$$

with

$$A_n^s = \frac{E_n^{s(0)} - \hbar\omega_c(n-1) - \hbar\omega_a/2}{\sqrt{\left(E_n^{s(0)} - \hbar\omega_c(n-1) - \hbar\omega_a/2\right)^2 + \hbar^2 g_R^2 n}}, \tag{13}$$

$$B_n^s = \frac{\hbar g_r\sqrt{n}}{\sqrt{\left(E_n^{s(0)} - \hbar\omega_c(n-1) - \hbar\omega_a/2\right)^2 + \hbar^2 g_R^2 n}}. \tag{14}$$

The pair $\{|n_s^{(0)}\rangle\}_{s=\pm}$ defines a two-dimensional manifold $\mathcal{E}_{\rm JC}(n)$, which is the set of states with a fixed number of excitations n (see Fig. 2). We denote it with the JC subscript, since the notion of manifold will be generalized in the perturbed picture.

In the perturbation Hamiltonian V, the counter-rotating term $H_{\rm CR}$ is described by the same coupling constant g_R as the interaction term of the unperturbed Hamiltonian $H_{\rm JC}$. However, the transition rates due to $H_{\rm CR}$ are much smaller far from the ultrastrong coupling regime $g_R \ll \omega$. Therefore perturbation theory is justified up to moderate coupling strengths (see Appendix A for quantitative details). We characterize the modified eigenstates of the time-independent perturbation theory up to second order, with the wave-function expansion given by

$$|n_s\rangle = \left|n_s^{(0)}\right\rangle + \left|n_s^{(1)}\right\rangle + \left|n_s^{(2)}\right\rangle. \tag{15}$$

The first-order correction reads

$$\left|n_s^{(1)}\right\rangle = \sum_{m\neq n}\sum_{\alpha=\pm}\frac{V_{mn}^{\alpha s}}{E_{nm}^{s\alpha}}\left|m_\alpha^{(0)}\right\rangle, \tag{16}$$

where $E_{nm}^{s\alpha} = E_n^{s(0)} - E_m^{\alpha(0)}$ and $V_{mn}^{\alpha s} = \langle m_\alpha^{(0)}|V|n_s^{(0)}\rangle$, namely,

$$\begin{aligned} V_{mn}^{\alpha s} = {} & \hbar g_R\left(\sqrt{n-1}B_n^s A_{n-2}^\alpha \delta_{m,n-2}\right. \\ & \left. + \sqrt{n+1}A_n^s B_{n+2}^\alpha \delta_{m,n+2}\right) \\ & + 2\hbar g_S B_m^\alpha B_n^s(\sqrt{n-1}\delta_{m,n-1} + \sqrt{n}\delta_{m,n+1}). \end{aligned} \tag{17}$$

The above equation shows that the perturbed eigenstates include states with $m = n \pm 1$ coupled by g_S and states with $m = n \pm 2$ coupled by g_R, which follows directly from the $H_{\rm AS}$ and $H_{\rm CR}$ Hamiltonians. The inclusion of the second-order correction leads to

$$\begin{aligned} |n_s\rangle = {} & \left(1 - \frac{1}{2}\sum_k\sum_{\alpha=\pm}\left(\frac{V_{nk}^{s\alpha}}{E_{nk}^{s\alpha}}\right)^2\right)\left|n_s^{(0)}\right\rangle \\ & + \sum_k\sum_{\alpha=\pm}\left(\frac{V_{kn}^{\alpha s}}{E_{nk}^{s\alpha}} + \sum_l\sum_{\beta=\pm}\frac{V_{kl}^{\alpha\beta}V_{ln}^{\beta s}}{E_{nk}^{s\alpha}E_{nl}^{s\beta}}\right)\left|k_\alpha^{(0)}\right\rangle. \end{aligned} \tag{18}$$

Based on the above result, we define the generalized (but always two-dimensional) manifolds $\mathcal{E}(n) = \{|n_s\rangle\}_{s=\pm}$. According to second-order perturbation, the eigenstate $|n_s\rangle$ includes contributions with different numbers of excitations $\{n, n\pm 1, \ldots, n\pm 4\}$, with the label n referring to the central component, which yields by far the leading contribution for weak enough coupling strengths $g_{R,S}$, for which the theory is applicable.

The correction V does not perturb the eigenvalues at the first order, because $V_{nn}^{s\sigma} = \langle n_s|V|n_\sigma\rangle = 0$. At the second order, the energy eigenvalues are $E_n^s = E_n^{s(0)} + E_n^{s(1)} + E_n^{s(2)}$, with $E_n^{s(1)} = 0$ and

$$E_n^{s(2)} = \sum_{k\neq n}\sum_{\alpha=\pm}\frac{\left(V_{kn}^{\alpha s}\right)^2}{E_{nk}^{s\alpha}}. \tag{19}$$

It is worth stressing that in the resonant and quasiresonant case, the nondimensional parameters that control the perturbative corrections induced by $H_{\rm CR}$ and $H_{\rm AS}$ are of order $g_R/(2\omega_c)$ and g_S/ω_c, respectively. Therefore, both corrections can be arbitrarily small, even in the case $g_S \simeq g_R$.

With the expressions (13), (14), and (17)–(19) at hand, we can now proceed to the main part of our analysis and examine the emission properties of the investigated system.

IV. FREQUENCY AND WEIGHT OF EMERGING TRANSITION LINES

A. Outcoupling Hamiltonian

In this section we assume the cavity mirrors to be semi-transparent so that the cavity mode described by a and $a^\dagger$ may exchange photons with an external reservoir:

$$H_{\rm ext} = \hbar\sqrt{\frac{\Gamma}{2\pi}}\int d\omega\sqrt{\mathcal{P}(\omega)}[ar^\dagger(\omega) + a^\dagger r(\omega)], \tag{20}$$

where the operators $r(\omega)$ and $r^\dagger(\omega)$ are related to orthogonal reservoir modes with energy $\hbar\omega$, and $\mathcal{P}(\omega)$ is a form factor that takes into account both the density of states and the energy dependence of the coupling, with $\mathcal{P}(\omega_c) = 1$. The constants are fixed in such a way that Γ coincides with the perturbative decay rate of a single-cavity photon towards the continuum,

$$\Gamma_{1\to 0} = \frac{2\pi}{\hbar^2}\int d\omega|\langle 0;\omega_R|H_{\rm ext}|1;0_R\rangle|^2\delta(\omega-\omega_c) = \Gamma, \tag{21}$$

with $|0_R\rangle$ standing for the reservoir vacuum, annihilated by all the r operators, and $|\omega_R\rangle = r^\dagger(\omega)|0_R\rangle$ being a generic single-photon state with a given energy ω, while the transition rate from the n-photon to the $(n-1)$-photon state of the cavity reads $\Gamma_{n\to n-1} = n\Gamma$.

B. Transition rate and emission spectrum

Here we will compute through the Fermi golden rule the decay rate and final photon energy distribution of the dressed atom-cavity states found in the previous section. In the perturbative regime, the transition from an initial state $|n_s\rangle$ to a final state $|n'_{s'}\rangle$, as defined in Eq. (18), corresponds to the transition frequency

$$\omega^{ss'}_{nn'} = \frac{E^s_n - E^{s'}_{n'}}{\hbar} \tag{22}$$

and is determined by the matrix elements

$$\langle n'_{s'};\omega_R|H_{\rm ext}|n_s;0_R\rangle = \hbar\sqrt{\frac{\Gamma}{2\pi}\mathcal{P}(\omega)}\,\langle n'_{s'}|a|n_s\rangle, \tag{23}$$

which are evaluated on-shell in the expression of the specific decay rate towards the channel $n'_{s'}$,

$$\Gamma^{ss'}_{nn'} = \Gamma|\langle n'_{s'}|a|n_s\rangle|^2\mathcal{P}\big(\omega^{ss'}_{nn'}\big), \tag{24}$$

that contributes to the total decay rate of the initial state,

$$\Gamma_{n,s} = \sum_{n',s'}\Gamma^{ss'}_{nn'} = \Gamma\sum_{n',s'}|\langle n'_{s'}|a|n_s\rangle|^2\mathcal{P}\big(\omega^{ss'}_{nn'}\big). \tag{25}$$

Notice that (i) the above expressions are valid provided that all the channels are characterized by different transition energies, otherwise interference effects occur; (ii) the form factor $\mathcal{P}$ must vanish for ω below the threshold for photon emission; and (iii) the state $|\omega_R\rangle$ in Eq. (23) carries a unit of $[\omega^{-1/2}]$, and $\mathcal{P}(\omega)$ is dimensionless. The specific and total decay rates also appear in the frequency distribution of the final photons, derived in Appendix B,

$$\begin{aligned} S_{n,s}(\omega) &= \sum_{n',s'} S^{ss'}_{nn'}(\omega) \\ &= \frac{\Gamma}{2\pi}\sum_{n',s'}\frac{|\langle n'_{s'}|a|n_s\rangle|^2\mathcal{P}\big(\omega^{ss'}_{nn'}\big)}{\big(\omega-\omega^{ss'}_{nn'}-\Delta_{n,s}\big)^2+\Gamma^2/4}, \end{aligned} \tag{26}$$

where $S^{ss'}_{nn'}(\omega)$ are specific spectral distributions related to a single decay channel. The spectral distribution is characterized by the presence of Lorentzian peaks around the transition frequencies, all shifted by

$$\Delta_{n,s} = \frac{\Gamma}{2\pi}\sum_{n',s'}|\langle n'_{s'}|a|n_s\rangle|^2\mathrm{P}\int d\omega\frac{\mathcal{P}(\omega)}{\omega-\omega^{ss'}_{nn'}}, \tag{27}$$

with $\mathrm{P}\int$ denoting principal value integration. The specific decay rates also determine the weight of each channel. Therefore the relevance of one channel compared to another one can crucially depend on the transition energy, through the form factor:

$$\frac{\Gamma^{ss'}_{nn'}}{\Gamma^{ss''}_{nn''}} = \frac{|\langle n'_{s'}|a|n_s\rangle|^2}{|\langle n''_{s''}|a|n_s\rangle|^2}\frac{\mathcal{P}\big(\omega^{ss'}_{nn'}\big)}{\mathcal{P}\big(\omega^{ss''}_{nn''}\big)}. \tag{28}$$

For example, the form factor can be characterized by a power-law behavior for the transition frequencies, $\mathcal{P}(\omega)\sim\omega^p$, as it occurs for free-space photons; in this case, lower-energy channels can be heavily hindered in favor of the higher-energy ones, despite being characterized by a larger matrix element of the operator a in Eq. (28). On the other hand, the relevance of a channel can be enhanced by engineering the continuum in order to obtain a form factor peaked around the frequency of interest: this can be done by coherently coupling the cavity mode with a single mode of a second cavity, broadened by losses towards free space.

C. Transition matrix element

The crucial quantity for contributions to both the transition rate $\Gamma^{ss'}_{nn'}$ and the emission spectrum $S^{ss'}_{nn'}(\omega)$ is the squared modulus of the transition element $\langle n'_{s'}|a|n_s\rangle$, which we shall now study in detail. Firstly, at the 0th order, i.e., without considering the perturbation Hamiltonian V [Eq. (6)], we find directly from Eq. (12)

$$\big|\big\langle n'^{(0)}_{s'}\big|a\big|n^{(0)}_s\big\rangle\big|^2 = \big|c^{s's}_n\big|^2\delta_{n',n-1} \tag{29}$$

with

$$c^{s's}_n = \sqrt{n}A^s_nA^{s'}_{n-1} + \sqrt{n-1}B^s_nB^{s'}_{n-1}. \tag{30}$$

This equation shows that only transitions between two "adjacent" manifolds $\mathcal{E}_{\rm JC}(n)$ and $\mathcal{E}_{\rm JC}(n-1)$ are allowed in the Jaynes-Cummings model, as expected.

The perturbation enriches the emission spectrum, as reported in Fig. 2 : both the permanent dipole moment related to the asymmetry of the atomic system and the counter-rotating terms give rise to additional transitions. In mathematical terms, this is expressed with additional Kronecker-δ terms in the transition element $|\langle n'_{s'}|a|n_s\rangle|^2$, accordingly scaled with the squared coupling constants g_S and g_R. In the perturbed expression for $|\langle n'_{s'}|a|n_s\rangle|^2$, obtained from the eigenstates $|n_s\rangle$

in Eq. (18), we consider all the correction terms up to second order in the coupling strengths g_R and g_S. Since $V_{nn}^{ss'} = 0$, the perturbed transition matrix element, including the aforementioned contributions, reads

$$|\langle n'_{s'}|a|n_s\rangle|^2 = (f^{\mathrm{JC}})_n^{s,s'}\delta_{n',n-1} + (f^{\mathrm{CR}})_n^{s,s'}\delta_{n',n-3} + \left(f_1^{\mathrm{A}}\right)_n^{s,s'}\delta_{n',n} + \left(f_2^{\mathrm{A}}\right)_n^{s,s'}\delta_{n',n-2}, \tag{31}$$

with coefficients

$$(f^{\mathrm{JC}})_n^{s,s'} = \left[1 - \sum_k \sum_{\alpha=\pm}\left(\left(\frac{V_{nk}^{s\alpha}}{E_{nk}^{s\alpha}}\right)^2 + \left(\frac{V_{n'k}^{s'\alpha}}{E_{n'k}^{s'\alpha}}\right)^2\right)\right]\left|c_n^{s's}\right|^2$$
$$+ 2c_n^{s's}\sum_k\sum_{\alpha,\beta=\pm}\left(\frac{V_{nk}^{\alpha\beta}V_{kn}^{\beta s}}{E_{nn}^{s\alpha}E_{nk}^{s\beta}}c_n^{s'\alpha} + \frac{V_{k-1,n-1}^{\alpha s'}}{E_{n-1,k-1}^{s'\alpha}}\frac{V_{kn}^{\beta s}}{E_{nk}^{s\beta}}c_k^{\alpha\beta} + \frac{V_{n-1,k}^{\alpha\beta}V_{k,n-1}^{\beta s'}}{E_{n-1,n-1}^{s'\alpha}E_{n-1,k}^{s'\beta}}c_n^{\alpha s}\right), \tag{32}$$

$$\left(f_1^{\mathrm{A}}\right)_n^{s,s'} = 4n|g_S|^2\left|B_n^s\sum_{\alpha=\pm}B_{n+1}^{\alpha}\left(\frac{c_{n+1}^{s'\alpha}}{E_{n,n+1}^{s\alpha}} + \frac{c_n^{\alpha s}}{E_{n,n+1}^{s'\alpha}}\right)\right|^2, \tag{33}$$

$$\left(f_2^{\mathrm{A}}\right)_n^{s,s'} = 4|g_S|^2\left|\sum_{\alpha=\pm}\left(\frac{c_{n+3}^{s'\alpha}}{E_{n,n+3}^{s\alpha}}B_{n+3}^{\alpha}B_n^s\sqrt{n-1} + \frac{c_n^{\alpha s}}{E_{n+2,n+1}^{s'\alpha}}B_{n+1}^{\alpha}B_{n+2}^s\sqrt{n+1}\right)\right|^2, \tag{34}$$

$$(f^{\mathrm{CR}})_n^{s,s'} = |g_R|^2\left|\sum_{\alpha=\pm}\left(\frac{c_{n+4}^{s'\alpha}}{E_{n,n+4}^{s\alpha}}\sqrt{n-1}B_n^sA_{n-2}^{\alpha} + \frac{c_n^{\alpha s}}{E_{n+3,n+1}^{s'\alpha}}\sqrt{n+2}B_{n+3}^sA_{n+1}^{\alpha}\right)\right|^2, \tag{35}$$

where $c_n^{ss'}$, defined in Eq. (30), does not depend on coupling constant g_S.

D. Discussion

The term f^{JC} describes the dominant contribution that arises from the Jaynes-Cummings model, perturbed by the second-order corrections. The coefficients f_1^{A} and f_2^{A} describe the transitions induced by the coupling g_S of light with the permanent dipole moment of the excited atomic level. Interestingly, f_1^{A} determines the strength of low-energy transitions, occurring within a fixed manifold $\mathcal{E}(n)$. On the other hand, transitions between the manifolds $\mathcal{E}(n)$ and $\mathcal{E}(n-2)$ are controlled by the terms in f_2^{A}. Finally, the coefficients f^{CR} describe the transitions between the manifolds $\mathcal{E}(n)$ and $\mathcal{E}(n-3)$ due to the counter-rotating terms in the perturbation Hamiltonian. This term arises in parallel with another one, which would correspond to transitions from the manifold $\mathcal{E}(n)$ to a higher-energy manifold $\mathcal{E}(n+1)$, that are not allowed in the perturbative regime. Note that the squared transition elements scale at the first approximation proportionally to the square of the coupling constants $g_{S/R}$, depending on the underlying transition mechanism. Further dependence on the coupling constant g_R is implicit in the B_n^s coefficient.

In this section we have shown that the inclusion of the perturbation Hamiltonian allows transitions to new manifolds. One might argue that closer manifolds are favorite, as JC transitions involve only adjacent manifolds, yielding a stronger contribution from the diagonal-coupling rather than the counter-rotating terms. On the other hand, transitions at higher frequencies can contribute with a higher intensity due to the larger form factor $\mathcal{P}$. Therefore, a quantitative comparison is needed to evaluate the spectrum and properly characterize the behavior in different regimes.

V. FORM FACTORS AND DOMINANT TRANSITIONS

In this section we analyze the transitions shown in Fig. 2, with a special emphasis on the ones induced by the perturbation Hamiltonian H_{AS} and H_{CR}. We will investigate relative emission strengths of transitions that origin from different Hamiltonian contributions as functions of the coupling constants $g_{R,S}$.

Figure 2 depicts the 13 allowed transitions from a given manifold $\mathcal{E}(n)$, respectively connecting manifolds $\mathcal{E}(n) \to \mathcal{E}(n-1)$ (JC interaction term, set of four green arrows at the left side), $\mathcal{E}(n) \to \mathcal{E}(n)$ and $\mathcal{E}(n) \to \mathcal{E}(n-2)$ (AS Hamiltonian, set of following five purple arrows), $\mathcal{E}(n) \to \mathcal{E}(n-3)$ (CR contribution, the last set of four red arrows). The transition frequencies will naturally depend on the coupling strength g_R, as in the Jaynes-Cummings theory, and weakly on g_S through second-order perturbation [Eq. (19)]. The Jaynes-Cummings energy structure is shown in Fig. 3 for manifolds $n = 7$ to $n = 10$, both in the resonant $\omega_c = \omega_a$ and detuned case $\omega_c - \omega_a = 0.2\,\omega_c$.

According to Eq. (26), the emission spectrum is approximately made up of a set of Lorentzian peaks. The structure is significantly enriched with respect to the typical Jaynes-Cummings case, with additional peaks emerging due to the presence of the Hamiltonian terms describing the asymmetric and counter-rotating contributions. Related photon emission rates may be comparable in strengths. Thus, the corresponding emission channels related to these peaks compete for a given initial excited state, mutually influencing the quantum yield related to different transitions. In Fig. 4 we separately plot the spectra for the initial states $|10_+\rangle$ (solid blue line) and $|10_-\rangle$ (dashed orange line), for the resonant case $\omega_a = \omega_c$ and fixed coupling strengths $g_R = g_S = 0.01\,\omega_c$. The spectra are plotted for two different form factors, $\mathcal{P} \propto \omega^2$ [Fig. 4(a)] and $\mathcal{P} = \mathrm{const}$ [Fig. 4(b)], corresponding respectively to three- and one-dimensional reservoir geometries in the case

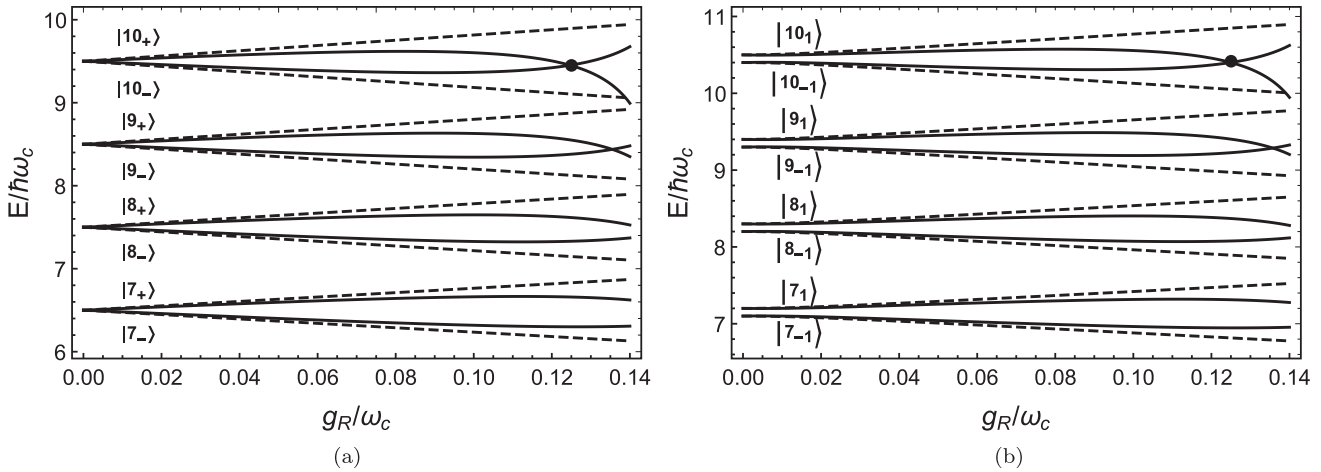

FIG. 3. Energy spectrum for $7 \leqslant n \leqslant 10$, including the second-order corrections (solid lines), computed for fixed $g_S/\omega_c = 0.1$ and varying g_R/ω_c, for (a) the resonant case $\omega_a = \omega_c$ and (b) the off-resonant case $(\omega_c - \omega_a)/\omega_c = 0.2$. The zeroth-order spectrum (dashed lines) is reported for comparison. The black dots at around $g_R = 0.125\,\omega_c$ indicate the first energy crossings. For coupling constants approaching these values, the structure of the energy ladder from Fig. 2 is no longer preserved, and higher-order perturbations are required for a consistent model.

of frequency-independent coupling between cavity and environment. The form factors are responsible for rescaling the relative strengths of the contributing peaks according to Eq. (26). The spectra and transition rates change smoothly for intermediate values of the parameter p. The single low-energy peak at around $\omega = 2\sqrt{10}g_R = 0.063\,\omega_c$ corresponds to the $|10_+\rangle \to |10_-\rangle$ transition induced by the inversion-symmetry breaking of the two-level system and might unveil applications for low-frequency sources. Therefore its tunability is an important feature: the position of this peak depends on g_S, i.e., on the permanent dipole moment $\boldsymbol{d}_{\rm ee}$ of the atom, and on the field strength in the cavity, related to the number of photons. In the classical limit, this provides an all-optical tuning possibility with the field amplitude [18]. Additionally, tuning could be achieved through orientation of the permanent dipole moment of the two-level system with an external DC electric field [21]. Around $\omega = \omega_c$ we recognize the Mollow triplet that arises from the JC interaction. Similar structures are repeated at around $\omega = 2\,\omega_c$ and $\omega = 3\,\omega_c$, arising respectively from the AS and CR Hamiltonian perturbations. Note that the positions of sidebands of the Mollow-like triplet at around $2\,\omega_c$ are related to the diagonal dipole moment and will accordingly be modified if g_S is tuned. We emphasize that all the peaks, including the Mollow-like sidebands, can be resolved in the spectra. In particular, even though the low-energy peak usually corresponds to the weakest transition intensities, it appears on top of a correspondingly suppressed background. As a consequence, the signal-to-noise ratio is found comparable for all emission peaks. Below we analyze the intensity ratio of different peaks depending on the coupling strengths of the model.

We study three selected transitions, representative for each Hamiltonian contribution, highlighted as thick arrows in Fig. 2: for the Jaynes-Cummings term we select the $|10_+\rangle \to |9_+\rangle$ transition; for the diagonal-coupling term the $|10_+\rangle \to |10_-\rangle$ transition; for the counter-rotating term the $|10_+\rangle \to |7_-\rangle$ transition, that corresponds to the highest frequency, and hence the most favored by form factors that increase with the energy of the emitted photon. In Fig. 5(a), we plot the squared matrix elements $|\langle n'_{s'}|a|n_s\rangle|^2$, which en-

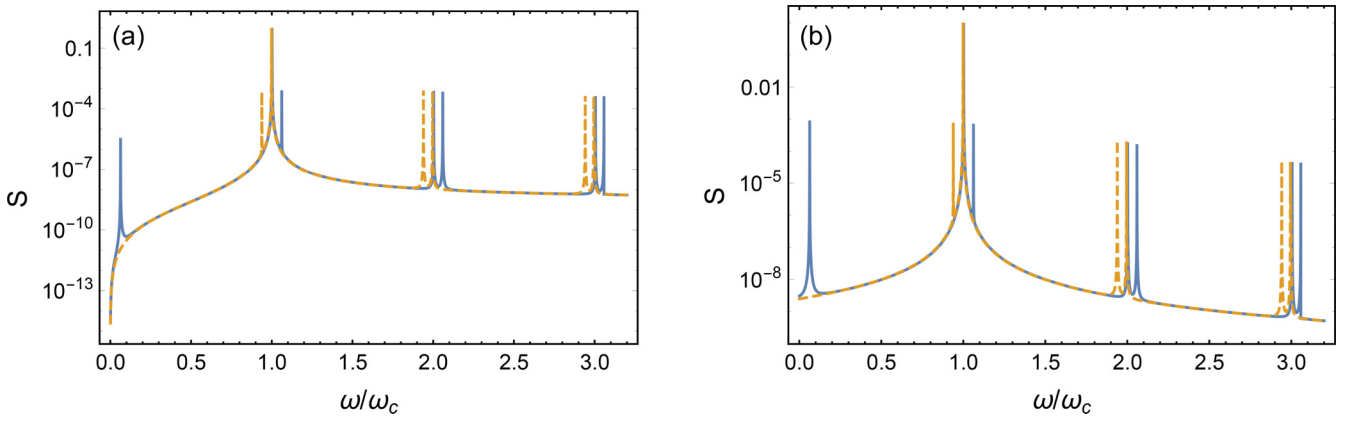

FIG. 4. Emission spectra (arbitrary units), computed according to Eq. (26) from the initial states $|10_+\rangle$ (solid blue line) and $|10_-\rangle$ (dashed orange line), with form factors scaling like ω^p, with (a) $p = 2$ and (b) and $p = 0$. Plots are normalized to the maximum of S, and we have set $\Gamma = 10^{-4}\omega_c$.

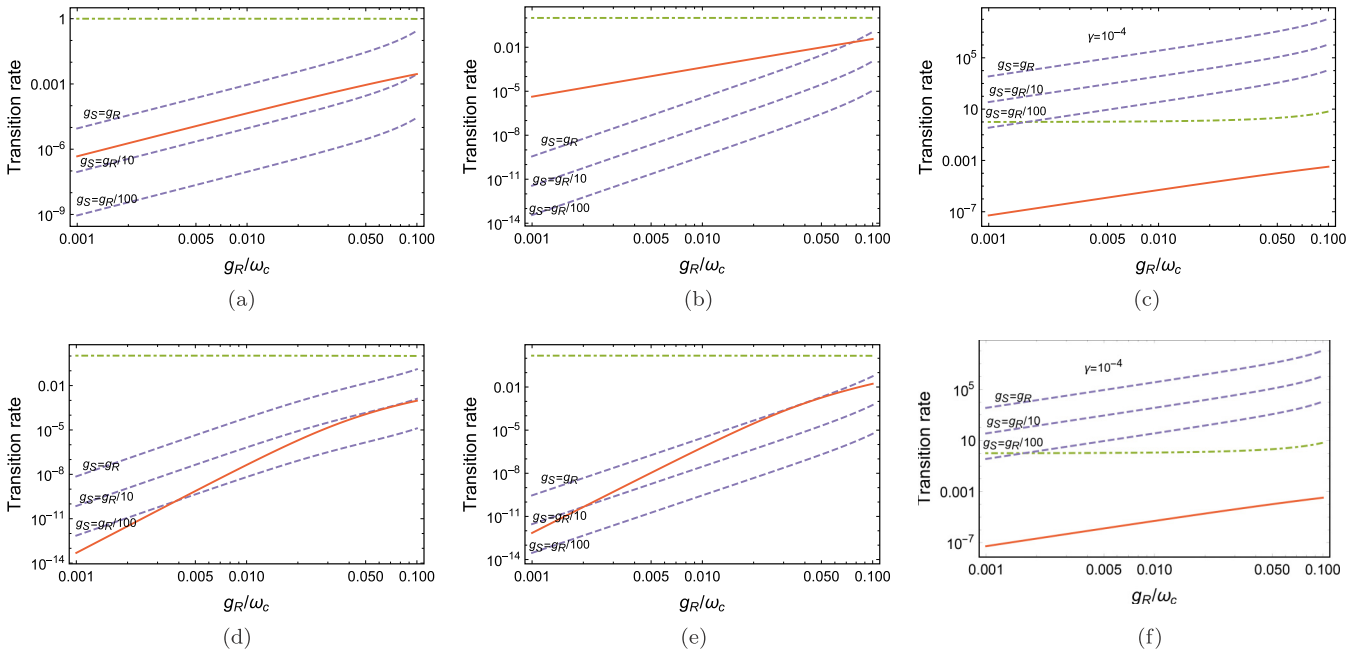

FIG. 5. Transition rates determined by a form factor $\mathcal{P} = \text{const}$ [panels (a) and (d)], $\mathcal{P} \propto \omega^2$ [panels (b) and (e)], and Lorentzian, centered at the frequency $\omega_{\text{ext}} = E^{+-}_{nn}/\hbar$, with a full width at half maximum $\gamma_{\text{ext}} = 10^{-4}\omega_{\text{ext}}$ [panels (c) and (f)]. Results are referred to the resonant $\omega_c = \omega_a$ [panels (a), (b), and (c)] and detuned case $(\omega_c - \omega_a)/\omega_c = 0.2$ [panels (d), (e), and (f)]. For each form factor, values on the vertical axis are normalized to the Jaynes-Cummings transition rate obtained in the limit $g_R \ll \omega_c$ for the resonant case. In panels (a) and (d), the plotted quantities correspond, up to a constant, to the squared matrix elements $|\langle n'_{s'}|a|n_s\rangle|^2$. Colors indicate different transition mechanisms: the Jaynes-Cummings transition $|10_+\rangle \to |9_+\rangle$ is plotted with a dot-dashed green line, the counter-rotating term $|10_+\rangle \to |7_-\rangle$ with a solid red line, and the transition driven by the diagonal coupling $|10_+\rangle \to |10_-\rangle$ with dashed violet lines, for three values of the diagonal-coupling strength, $g_S = g_R, g_R/10, g_R/100$.

tirely determine the relative weight of the different decay channels in the case of a constant form factor [see Eq. (28)]. They are plotted separately for each considered transition. As anticipated, the contribution due to the Jaynes-Cummings interaction dominates, overcoming the other terms by several orders of magnitude for the investigated range of coupling strengths g_R. As expected, the JC contribution has a relatively weak dependence on g_R, which induces small corrections to the zeroth-order result (see Fig. 3). The purple (red) lines in Fig. 5 represent the contributions determined by the AS (CR) Hamiltonian. Results obtained for the different values $g_S = g_R,\ g_R/10,\ g_R/100$ are presented. This confirms the intuition suggested at the end of the previous section, that for equal coupling strengths $g_S = g_R$ the term induced by the diagonal coupling overcomes the counter-rotating contribution. Both terms share the same linear scaling with their respective coupling strengths g_S or g_R, so, as we decrease g_S, the squared transition amplitude $|\langle n_{s'}|a|n_s\rangle|^2$ is gradually suppressed.

This simple linear scaling is slightly modified in the detuned case, in which the slopes change at around $g_R \simeq (\omega_c - \omega_a)/2\sqrt{n}$. An example for a strong detuning $\omega_a = 0.8\,\omega_c$ is shown in Fig. 5(d). We find that in this case the contribution of both perturbative terms is suppressed with respect to the resonant contribution. However, for relatively small coupling strengths ($g_R < 4 \times 10^{-3}\,\omega_c$) the terms corresponding to the asymmetric contribution still dominate over those due to the counter-rotating Hamiltonian, even for small $g_S = 0.01 g_R$. For a wide range of coupling strengths, the squared transition amplitudes induced by the perturbation related to the asymmetry dominate over those originating from the counter-rotating term. However, if the outcoupling Hamiltonian H_{ext} involves a form factor scaling as ω^p, the weight of a decay channel is proportional to the pth power of the transition frequency. Therefore, in a 3D continuum geometry in which the density of states scales as ω^2, the relevance of low-energy transitions tends to be suppressed. We show this case in both the resonant and off-resonant case in Figs. 5(b)–5(e). In the off-resonant case, we note that for equal coupling strengths $g_S = g_R$ the terms originating from the diagonal coupling still dominate over the counter-rotating ones, despite the latter being by far energetically favored. Panels (a), (b), (d), and (e) of Fig. 5 show the changes in the hierarchy between low-energy decays, determined by the asymmetric perturbation, and high-energy transitions due to counter-rotating terms, in the cases of constant and quadratic form factor $\mathcal{P}$. The results, determined by Eq. (25), show that it is not generally justified to study the intrinsic asymmetry effects of the atomic levels while neglecting the counter-rotating contributions, since the effects entailed by these two kinds of corrections compete with each other. In particular, high-energy transitions entailed by the counter-rotating Hamiltonian can be overwhelmingly relevant in the case of a form factor that increases with energy. However, the different behavior of transition rates according to Eq. (28),

$$\Gamma^{ss'}_{nn'} \propto |\langle n'_{s'}|a|n_s\rangle|^2 \mathcal{P}\left(\omega^{ss'}_{nn'}\right), \tag{36}$$

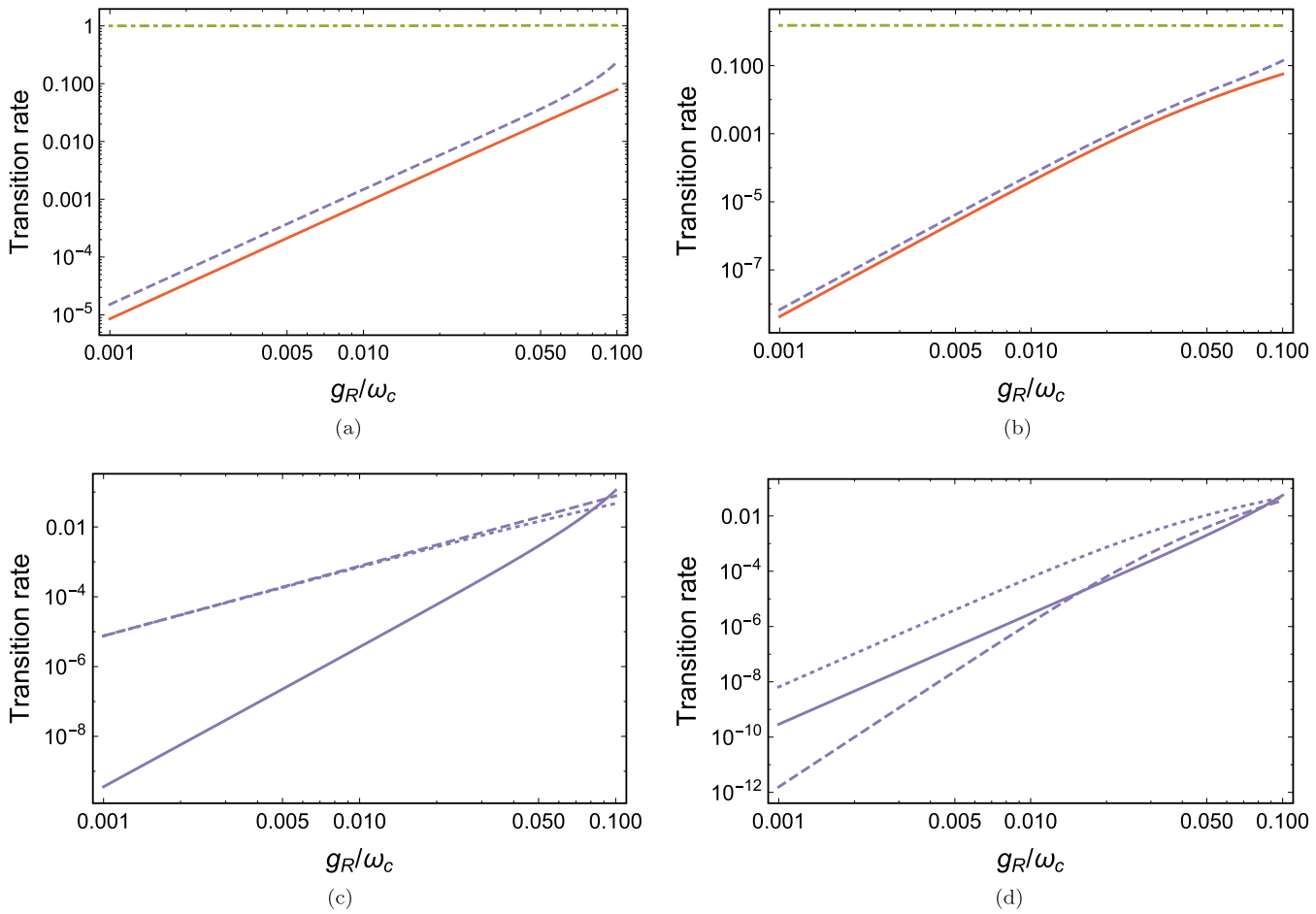

FIG. 6. Total transition rates according to Eq. (24) for each Hamiltonian contribution, for a fixed initial state $|10_+\rangle$: rate of the Jaynes-Cummings transitions $\Gamma^{\rm JC}_{10,+} = \Gamma^{++}_{10,9} + \Gamma^{+-}_{10,9}$ (dot-dashed green line), diagonal-coupling mechanism $\Gamma^{\rm AS}_{10,+} = \Gamma^{++}_{10,8} + \Gamma^{+-}_{10,8} + \Gamma^{+-}_{10,10}$ (dashed violet line), and the counter-rotating transitions $\Gamma^{\rm CR}_{10,+} = \Gamma^{++}_{10,7} + \Gamma^{+-}_{10,7}$ (solid red line) (a) on resonance and (b) for the detuned case. Individual contributions to the diagonal coupling are resolved in panels (c) and (d) for the resonant and the detuned case, respectively, where the solid line represents the low-energy transition rate $\Gamma^{+-}_{10,10}$, while the dashed ($\Gamma^{++}_{10,8}$) and dotted ($\Gamma^{+-}_{10,8}$) lines correspond to transitions around $2\,\omega_c$. In each plot, $g_S = g_R$ and the form factor is $\mathcal{P} = \text{const}$. Values on the vertical axis are normalized to the Jaynes-Cummings transition rate obtained in the limit $g_R \ll \omega_c$ for the resonant case.

in the cases of constant $\mathcal{P}$ [Figs. 5(a) and 5(d)] and $\mathcal{P} \propto \omega^2$ [Figs. 5(b) and 5(e)] suggests the possibility of tailoring the weight of transition lines by engineering the density of states $\mathcal{P}(\omega)$ of the external field, e.g., in the form of a Lorentzian, centered on the frequency $\omega^{+-}_{n,n}$, as follows:

$$\mathcal{P}(\omega) \propto \frac{\gamma_{\rm ext}/(2\pi)}{(\omega - \omega^{+-}_{nn} - \Delta_{n,+})^2 + \gamma^2_{\rm ext}/4}. \tag{37}$$

Therefore we couple the atom-cavity system to a single-mode cavity, assuming that the form factor $\mathcal{P}$ is a Lorentzian function centered at the low-energy transition frequency $\omega_{\rm ext} = \omega^{+-}_{10,10}$ and characterized by a full-width at half-maximum $\gamma_{\rm ext} = 10^{-4}\omega_c$. The cavity is tailored to emphasize the strength of the low-energy transition $|n_+\rangle \to |n_-\rangle$ at the cost of suppressing other transitions. Indeed, as demonstrated in Figs. 5(c) and 5(f), this is successful in both the resonant and the detuned case. A cavity with similar parameters can be realized in photonic crystals [26] that provide one- or two-dimensional photonic environments, in whispering-gallery-mode resonators [27] or, with smaller quality factors, using metamaterials [28]. Notice that the advantage entailed by the form factor (36) in selecting the low-energy transition is effective only if $\gamma_{\rm ext} \ll \omega_c$; when the width of the Lorentzian becomes comparable to ω_c, the results tend to approach those obtained for a constant form factor.

For the above analysis we have selected only one exemplary transition of the Jaynes-Cummings diagonal-coupling and counter-rotating groups, corresponding to arrows with different colors in Fig. 2. In Fig. 6 we show the total transition rates in each group, considering the initial state $|n_s\rangle = |10_+\rangle$. The dot-dashed green lines correspond to the total rate of the Jaynes-Cummings transitions $\Gamma^{\rm JC}_{10,+} = \Gamma^{++}_{10,9} + \Gamma^{+-}_{10,9}$, the dashed purple lines to the diagonal coupling $\Gamma^{\rm AS}_{10,+} = \Gamma^{++}_{10,8} + \Gamma^{+-}_{10,8} + \Gamma^{+-}_{10,10}$, and the solid red lines to the counter-rotating contribution $\Gamma^{\rm CR}_{10,+} = \Gamma^{++}_{10,7} + \Gamma^{+-}_{10,7}$. We find that, as expected, the higher-energy contributions from the asymmetric Hamiltonian $H_{\rm AS}$ around $2\,\omega_c$ are strong enough to overcome the ones induced by the counter-rotating terms. This can be also seen from Fig. 6(c), in which we resolve different contributions induced by $H_{\rm AS}$ in the decay from the state $|10_+\rangle$.

The difference between the two perturbative contributions becomes even smaller in the detuned case, in which all perturbative terms are suppressed, as can be seen from panels (b) and (d) in Fig. 6. One can notice from Fig. 6(c) that the $|n_+\rangle \to |n_-\rangle$ transition within the same manifold (see thicker purple line in Fig. 2) has the lowest intensity compared to the other transitions $|n_\pm\rangle \to |(n-2)_\pm\rangle$ for $g_R < 0.05\omega_c$. This demonstrates that the low-energy transition competes even with higher-energy transitions that originate from the same Hamiltonian term $H_{\rm AS}$. However, a Lorentzian form factor centered around the low-energy transition allows us to avoid also this competition. Interestingly, as shown Fig. 5(d), for the detuned case the asymmetric contributions are comparable with each other for all considered values of the coupling constant and are more stable when varying the detuning parameter.

VI. CONCLUSIONS

We have investigated the emission properties of a two-level system coupled to a single-mode electromagnetic field, including interaction channels based on the Jaynes-Cummings, counter-rotating and asymmetry-related contributions. In the electric-dipole interaction mechanism, the first two interactions arise from the coupling of the field mode with the induced transition dipole moment, while the latter requires a permanent dipole characterizing the system's eigenstates. Light-matter coupling with permanent dipoles gives birth to additional emission peaks. We have demonstrated that even though at some frequencies the asymmetry-related contribution is weak in relative terms, the signal-to-noise ratio is comparable for all emission peaks. Therefore all the Hamiltonian terms contribute to the emission spectrum: in particular, they induce multiple active light emission channels, none of which can *a priori* be neglected in a general analysis. However, the relative strengths of the emission peaks can be modified with a suitable photonic environment. A properly chosen function for the density of states would allow one to funnel the emitted energy into the desired channel. From an application point of view, an appealing possibility is related to enhancing the low-energy transition between the states of the same manifold. On the cavity-atomic system resonance, the frequency of this particular transition scales linearly with the coupling strength g_R and is of the same order of magnitude, i.e., typically much lower than the cavity frequency C. This feature could be exploited to generate low-frequency radiation, that for different atomic systems might span across the MHz–THz regimes, in particular, with the application to bridge the THz gap. We have demonstrated this possibility exploiting a Lorentzian form factor, showing that for the external cavity parameters that lie well within the range of experimental capabilities, the asymmetry-related emission channel may even become dominant.

ACKNOWLEDGMENTS

We acknowledge the PROM project at the Nicolaus Copernicus University in Toruń. G.S. is supported by the International Centre for Theory of Quantum Technologies project (Contract No. 2018/MAB/5), carried out within the International Research Agendas Programme of the Foundation for Polish Science, cofinanced by the European Union from the funds of the Smart Growth Operational Programme, Axis IV: Increasing the research potential (Measure 4.3). K.S. is supported by the Polish National Science Centre, Project No. 2018/31/D/ST3/01487. P.F. and S.P. acknowledge support by MIUR via PRIN 2017 (Progetto di Ricerca di Interesse Nazionale), project QUSHIP (2017SRNBRK). P.F. was partially supported by the Italian National Group of Mathematical Physics (GNFM-INdAM). P.F., S.P., and F.V.P. were partially supported by Istituto Nazionale di Fisica Nucleare (INFN) through the project "QUANTUM" and by Regione Puglia and QuantERA ERA-NET Cofund in Quantum Technologies (GA No. 731473), project PACE-IN.

APPENDIX A: VALIDITY OF THE PERTURBATIVE APPROACH

In this Appendix we discuss the range of coupling strengths for which the perturbative approach used in the main text is justified. The condition for the analysis to be consistent is that the perturbation series converge both for the perturbed energies and states. This is not the case around energy crossings, where some of the series terms in the perturbed eigenstate given by Eq. (18) diverge. On the other hand, sufficiently away from energy crossing the state norm is approximately preserved. To identify the applicability range of the approach, we therefore verify the normalization of states.

For the cases investigated in the main manuscript, the first energy crossing among the investigated states appears for those corresponding to the highest manifold. In Fig. 7 we plot the norm of state $|10_+\rangle$ as a function of $g_S = g_R$. A clear divergence appears for coupling strengths approaching $0.14\,\omega_c$, which results from a crossing involving higher manifolds, in this case up to $\mathcal{E}(14)$. The vertical line in the figure indicates the limit for the coupling strengths considered in the main text.

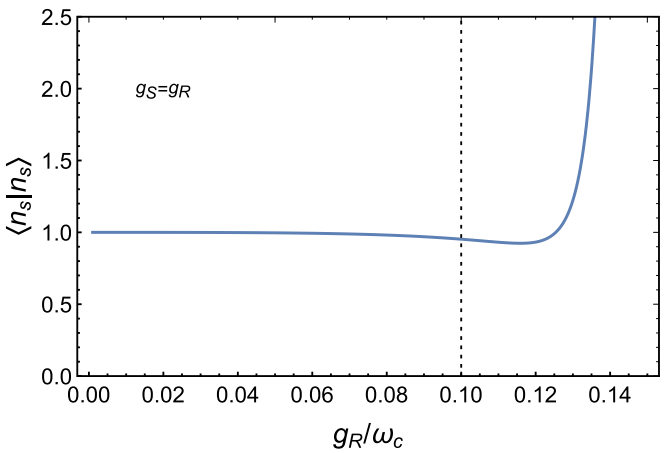

FIG. 7. Norm of state $|10_+\rangle$, as obtained from Eq. (18). For coupling strengths exceeding $g_R \simeq 0.1\,\omega_c$ the norm deviates from 1, which is an indication of the breakdown of perturbation theory.

APPENDIX B: SPECTRAL DISTRIBUTION OF EMITTED PHOTONS

In order to derive Eqs. (24)–(26), let us consider an initial state $|\psi_0\rangle$, evolving under the Hamiltonian $H = H_0 + H_{\rm int}$, where $H_{\rm int}$ is meant as a perturbation of the "free" Hamiltonian H_0. While

$$H_0|\psi_0\rangle = E_0|\psi_0\rangle, \tag{B1}$$

the presence of the interaction Hamiltonian $H_{\rm int}$ makes the initial state unstable, inducing decay towards generalized eigenstates $|q\rangle$ of H_0 (where q is generally a multi-index of N quantum numbers, some of which can be discrete, such as spin or polarization), satisfying

$$H_0|q\rangle = E(q)|q\rangle. \tag{B2}$$

The probability associated to a specific q at an arbitrary time t can be computed by projecting $|q\rangle$ on the evolved state $|\psi(t)\rangle = \exp(-iHt)|\psi\rangle$ of the system, determined by the corresponding matrix element of the resolvent $(z-H)^{-1}$ through a Fourier-Laplace transform:

$$\mathcal{A}(q,t) = \langle q|e^{-iHt/\hbar}|\psi_0\rangle = \frac{i}{2\pi}\int_{\mathcal{B}} dz\, e^{-izt/\hbar}\langle q|\frac{1}{z-H}|\psi_0\rangle, \tag{B3}$$

where $\mathcal{B} = (-\infty + i\eta, +\infty + i\eta)$ is an arbitrary line, parallel to the real axis, with $\eta > 0$. Therefore, in order to characterize the matrix element of the resolvent, it is sufficient to determine the amplitude and probability associated to the distribution of decay products. In particular, we are interested in the asymptotic distribution

$$P_\infty(q) = \lim_{t\to\infty} |\langle q|e^{-iHt/\hbar}|\psi_0\rangle|^2. \tag{B4}$$

For $\mathrm{Im}(z) \neq 0$, the resolvent satisfies the equation

$$\frac{1}{z-H} = \frac{1}{z-H_0} + \frac{1}{z-H_0}H_{\rm int}\frac{1}{z-H}, \tag{B5}$$

that can be used, along with the assumption $\langle\psi_0|H_{\rm int}|\psi_0\rangle$, to determine an approximate form of the matrix element appearing in the right-hand side of (B3),

$$\langle q|\frac{1}{z-H}|\psi_0\rangle \simeq \frac{1}{z-E(q)}\langle q|H_{\rm int}|\psi_0\rangle\langle\psi_0|\frac{1}{z-H}|\psi_0\rangle, \tag{B6}$$

where the corrections are $O(H_{\rm int}^2)$ and proportional to the matrix elements $\langle q|H_{\rm int}|q'\rangle$. An error of the same order on $\mathcal{A}(q,t)$ is entailed by applying the Weisskopf-Wigner approximation to the initial state propagator,

$$\langle\psi_0|\frac{1}{z-H}|\psi_0\rangle \simeq \frac{1}{z-(E_0+\hbar\Delta-i\hbar\Gamma/2)}, \tag{B7}$$

with

$$\Delta = \frac{1}{\hbar}\mathrm{P}\int d^N q\, \frac{|\langle q|H_{\rm int}|\psi_0\rangle|^2}{E_0 - E(q)}, \tag{B8}$$

$$\Gamma = \frac{2\pi}{\hbar}\int d^N q\, |\langle q|H_{\rm int}|\psi_0\rangle|^2\delta(E_0 - E(q)), \tag{B9}$$

which yields an expression of the transition amplitude in terms of a solvable integral

$$\mathcal{A}(q,t) \simeq \frac{i}{2\pi}\int_{\mathcal{B}} dz\, \frac{\langle q|H_{\rm int}|\psi_0\rangle e^{-izt/\hbar}}{(z-E(q))[z-(E_0+\hbar\Delta-i\hbar\Gamma/2)]}, \tag{B10}$$

leading to the asymptotic distribution

$$P_\infty(q) \simeq \frac{|\langle q|H_{\rm int}|0\rangle|^2}{(E(q)-E_0-\hbar\Delta)^2 + \hbar^2\frac{\Gamma^2}{4}}. \tag{B11}$$

Suppose now that the final states $|q\rangle$ can be collected in different decay channels, namely, orthogonal subspaces $\mathcal{D}_j$ of final products, identified by quantum numbers belonging to specific domains D_j. The energy distribution associated to the decay channel n reads

$$\begin{aligned} P_\infty^{(j)}(E) &= \int_{D_j} d^N q\, \delta(E - E(q))P_\infty(q) \\ &\simeq \frac{1}{2\pi}\frac{\hbar\Gamma_j}{(E-E_0-\hbar\Delta)^2 + \hbar^2\frac{\Gamma^2}{4}}, \end{aligned} \tag{B12}$$

with

$$\Gamma_j = \frac{2\pi}{\hbar}\int_{D_j} d^N q\, |\langle q|H_{\rm int}|\psi_0\rangle|^2\delta(E_0 - E(q)), \tag{B13}$$

the channel decay rate. Computation of the total probability for the system to decay in channel n yields the classical result

$$p^{(j)} = \int dE P_\infty^{(j)}(E) \simeq \frac{\Gamma_j}{\Gamma}. \tag{B14}$$

If the decay channels are represented by states $|j\rangle \otimes |\omega\rangle$, in which a photon of frequency ω is emitted by a bound system in the transition from an initial state $|i\rangle$ of energy $\hbar\omega_i$ towards a specific final state $|j\rangle$ of energy $\hbar\omega_j$, the spectral distribution of final states can be conveniently represented in terms of the photon frequency,

$$\begin{aligned} S^{(j)}(\omega) &= \hbar P_\infty^{(j)}[\hbar(\omega_j + \omega)] \\ &\simeq \frac{1}{2\pi}\frac{\Gamma_j}{[\omega - (\omega_i - \omega_j + \Delta)]^2 + \frac{\Gamma^2}{4}}, \end{aligned} \tag{B15}$$

which corresponds to the quantity in Eq. (26).

[1] Q. Xie, H. Zhong, M. T. Batchelor, and C. Lee, The quantum Rabi model: Solution and dynamics, J. Phys. A: Math. Theor. **50**, 113001 (2017).

[2] B. W. Shore and P. L. Knight, The Jaynes-Cummings model, J. Mod. Opt. **40**, 1195 (1993).

[3] P. Forn-Díaz, L. Lamata, E. Rico, J. Kono, and E. Solano, Ultrastrong coupling regimes of light-matter interaction, Rev. Mod. Phys. **91**, 025005 (2019).

[4] J. Bourassa, J. M. Gambetta, A. A. Abdumalikov, Jr., O. Astafiev, Y. Nakamura, and A. Blais, Ultrastrong coupling

regime of cavity QED with phase-biased flux qubits, Phys. Rev. A **80**, 032109 (2009).

[5] T. Niemczyk, F. Deppe, H. Huebl, E. Menzel, F. Hocke, M. Schwarz, J. Garcia-Ripoll, D. Zueco, T. Hümmer, E. Solano, *et al.*, Circuit quantum electrodynamics in the ultrastrong-coupling regime, Nat. Phys. **6**, 772 (2010).

[6] G. Günter, A. A. Anappara, J. Hees, A. Sell, G. Biasiol, L. Sorba, S. De Liberato, C. Ciuti, A. Tredicucci, A. Leitenstorfer *et al.*, Sub-cycle switch-on of ultrastrong light–matter interaction, Nature (London) **458**, 178 (2009).

[7] Q. Zhang, M. Lou, X. Li, J. L. Reno, W. Pan, J. D. Watson, M. J. Manfra, and J. Kono, Collective non-perturbative coupling of 2D electrons with high-quality-factor terahertz cavity photons, Nat. Phys. **12**, 1005 (2016).

[8] A. Crespi, S. Longhi, and R. Osellame, Photonic Realization of the Quantum Rabi Model, Phys. Rev. Lett. **108**, 163601 (2012).

[9] J. George, T. Chervy, A. Shalabney, E. Devaux, H. Hiura, C. Genet, and T. W. Ebbesen, Multiple Rabi Splittings under Ultrastrong Vibrational Coupling, Phys. Rev. Lett. **117**, 153601 (2016).

[10] P. Schneeweiss, A. Dareau, and C. Sayrin, Cold-atom-based implementation of the quantum Rabi model, Phys. Rev. A **98**, 021801(R) (2018).

[11] D. Braak, Integrability of the Rabi Model, Phys. Rev. Lett. **107**, 100401 (2011).

[12] Q.-H. Chen, C. Wang, S. He, T. Liu, and K.-L. Wang, Exact solvability of the quantum Rabi model using Bogoliubov operators, Phys. Rev. A **86**, 023822 (2012).

[13] R. Silbey and R. A. Harris, Variational calculation of the dynamics of a two level system interacting with a bath, J. Chem. Phys. **80**, 2615 (1984).

[14] H. Zheng, S. Y. Zhu, and M. S. Zubairy, Quantum Zeno and Anti-Zeno Effects: Without the Rotating-Wave Approximation, Phys. Rev. Lett. **101**, 200404 (2008).

[15] E. K. Irish, Generalized Rotating-Wave Approximation for Arbitrarily Large Coupling, Phys. Rev. Lett. **99**, 173601 (2007).

[16] S. He, C. Wang, Q.-H. Chen, X.-Z. Ren, T. Liu, and K.-L. Wang, First-order corrections to the rotating-wave approximation in the Jaynes-Cummings model, Phys. Rev. A **86**, 033837 (2012).

[17] I. G. Savenko, O. V. Kibis, and I. A. Shelykh, Asymmetric quantum dot in a microcavity as a nonlinear optical element, Phys. Rev. A **85**, 053818 (2012).

[18] O. V. Kibis, G. Y. Slepyan, S. A. Maksimenko, and A. Hoffmann, Matter Coupling to Strong Electromagnetic Fields in Two-Level Quantum Systems with Broken Inversion Symmetry, Phys. Rev. Lett. **102**, 023601 (2009).

[19] E. Paspalakis, J. Boviatsis, and S. Baskoutas, Effects of probe field intensity in nonlinear optical processes in asymmetric semiconductor quantum dots, J. Appl. Phys. **114**, 153107 (2013).

[20] I. Y. Chestnov, V. A. Shahnazaryan, A. P. Alodjants, and I. A. Shelykh, Terahertz lasing in ensemble of asymmetric quantum dots, ACS Photonics **4**, 2726 (2017).

[21] P. Gładysz, P. Wcisło, and K. Słowik, Propagation of optically tunable coherent radiation in a gas of polar molecules, Sci. Rep. **10**, 1 (2020).

[22] M. Koppenhöfer and M. Marthaler, Creation of a squeezed photon distribution using artificial atoms with broken inversion symmetry, Phys. Rev. A **93**, 023831 (2016).

[23] M. A. Antón, S. Maede-Razavi, F. Carreno, I. Thanopulos, and E. Paspalakis, Optical and microwave control of resonance fluorescence and squeezing spectra in a polar molecule, Phys. Rev. A **96**, 063812 (2017).

[24] L.-T. Shen, Z.-B. Yang, H.-Z. Wu, and S.-B. Zheng, Ground state of an ultrastrongly coupled qubit-oscillator system with broken inversion symmetry, Phys. Rev. A **93**, 063837 (2016).

[25] G. Scala, F. V. Pepe, P. Facchi, S. Pascazio, and K. Słowik, Light interaction with extended quantum systems in dispersive media, New J. Phys. **22**, 123047 (2020).

[26] Q. Lu, X. Chen, C.-L. Zou, and S. Xie, Extreme terahertz electric-field enhancement in high-Q photonic crystal slab cavity with nanoholes, Opt. Express **26**, 30851 (2018).

[27] D. W. Vogt and R. Leonhardt, Ultra-high Q terahertz whispering-gallery modes in a silicon resonator, APL Photonics **3**, 051702 (2018).

[28] D. C. Zografopoulos and R. Beccherelli, Tunable terahertz fishnet metamaterials based on thin nematic liquid crystal layers for fast switching, Sci. Rep. **5**, 13137 (2015).